Multiscale modeling of ion diffusion in cement paste: electrical double layer effects

Yuankai Yang[(1)], Ravi A. Patel[(2)], Sergey V. Churakov[(2,3),‡], Nikolaos I. Prasianakis[(2)], Georg Kosakowski[(2)] and Moran Wang[(1),†]

(1) Department of Engineering Mechanics and CNMM, Tsinghua University, Beijing 100084, China

(2) Laboratory for Waste Management, Paul Scherrer Institute, Villigen 5232, Switzerland

(3) Institute of Geological Sciences, University of Bern, Bern 3012, Switzerland

Abstract

Understanding the mechanism of ion diffusion in hardened cement paste is of great importance for predicting long-term durability of concrete structures. Gel pores in calcium silicate hydrate (C-S-H) phase forms dominant pathway for transport in cement paste with low w/c ratios where the electrical double layer effects play an important role. Experimental results suggest that the effective diffusivity of chloride ions is similar as that of tritiated water (HTO) and higher than the sodium ions. This difference can be attributed to the electrical double layer near the charged C-S-H surfaces. In order to understand species transport processes in C-S-H and to quantify its effective diffusivity, a multiscale modelling technique has been proposed to combine atomic-scale and pore-scale modeling. At the pore-scale, the lattice Boltzmann method is used to solve a modified Nernst Planck equation to model transport of ions in gel pores. The modified Nernst Planck equation accounts for steric and ion-ion correlation effects by using correction term for excess chemical potential computed using the results from the grand canonical Monte Carlo scheme at atomic scale and in turn bridges atomic scale model with pore scale model. Quantitative analysis of pore size influence on effective diffusivity carried out by this multiscale model shows that the contribution of the Stern layer to ion transport is not negligible for pores with diameter less than 10 nm. The developed model is able to reproduce qualitatively the trends of the diffusivity of different ions reported in literature.

***Keywords*:** multiscale modeling; effective diffusivity; electrical double layer; C-S-H

† Corresponding author, Email: mrwang@tsinghua.edu.cn

‡ Corresponding author, Email: sergey.churakov@psi.ch

1. Introduction

The ability of ion to transport through cementitious materials influences the extent of several degradation mechanisms such as sulphate attack, carbonation, leaching, chloride transport in marine structures and contaminant transport in hazardous waste disposal systems. Therefore, improving the understanding of the ion transport mechanisms through cementitious materials is of great importance for predicting the long-term performance and service life of concrete structures. In the absence of pressure gradient (advection), diffusion is the key transport ion mechanism in cementitious materials which can be characterized by the effective diffusivity of the media. The pore space for ion diffusion in cement paste can be distinguished (in absence of defects such as micro-cracks) into capillary pores, submicron capillary and gel pores in calcium silicate hydrate (C-S-H) phase. The dominant pore space can be distinguished using the concept of capillary pore percolation [1]. When the capillary porosity depercolates, the gel pores in calcium silicate hydrate (C-S-H) phase forms the dominant pathway for transport in cement paste [2]. At this stage nano-scale effects on ion transport would play important role.

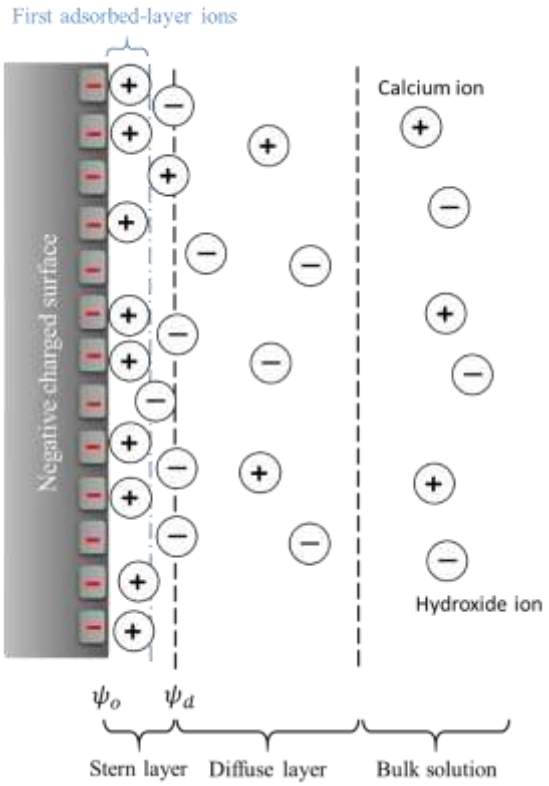

Fig. 1 A sketch of the structure of electrical double layer near the charged C-S-H surface. The pore solution is $Ca(OH)_2$. In the high-*p*H pore solution, the C-S-H surface is usually negative charged, but the bivalent calcium ions can over balance the negative charge on the surface, which cause the positive zeta potential ψ_d. This phenomenon is named as charge reversal [3].

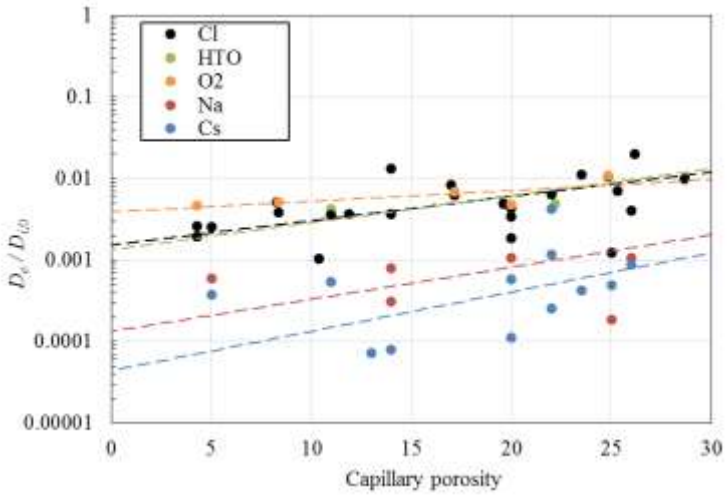

Fig. 2 The relative effective diffusion coefficients of Na^+, Cl^-, Cs^+, dissolved O_2 and HTO in saturated CEM I cement paste with respect to the capillary porosity. Different colors represent each species shown in legend. The points are experiment data collected from references [4-17] (see detail in Appendix) and the lines for each species are given by the best fitting. $D_{i,0}$ is the species diffusivity in free water [18, 19]: $D_0 = 2.2\ \mu m^2/ms$ of HTO and O_2; $D_0 = 2.0\ \mu m^2/ms$ of Cl^- and Cs^+; $D_0 = 1.3\ \mu m^2/ms$ of Na^+.

59 The surface of C-S-H carries negative charge as in contact with the high-*p*H electrolyte
60 [20]. The ions in the pore solution interact with the charged surface and form the
61 electrical double layer (EDL) structure near the surface depicted in Fig. 1 [21]. The
62 bivalent calcium ions can over balance the negative charge on the surface, which cause
63 the positive zeta potential ψ_d. This phenomenon is named as charge reversal [3].The
64 influence of EDL is dominant in pores of few nano-meter width and in case of
65 compacted clays it has been reported that EDL can enhance sodium transport but reduce
66 chloride transport [22]. Through a calibrated electronic spin resonance (ESR)
67 experiment, the major mean sizes of gel pore are 1.8 and 7.0 nanometers [23], which is
68 comparable with EDL thickness [24], therefore the ion-surface interaction is strong
69 enough and the electrokinetic effect should be respected as shown by Appelo [25] and
70 Yang & Wang [24]. However, the effect of EDL on ion transport in cement-paste is not
71 widely studied. A collection of diffusivity of different ionic species collected from
72 literature [4-17] (the values are tabulated in Appendix) is plotted in Fig. 2. It clearly
73 shows that significant differences exist between relative diffusivity of different species
74 in cement paste with diffusivity of Cl^- equal to that of uncharged tracers HTO/O_2 which
75 is higher than Na^+ and Cs^+ following the order $Cl^- \approx HTO/O_2 > Na^+ > Cs^+$. These
76 differences are significant at low capillary porosities which further strengthen the
77 hypothesis that effect of EDL on ion transport cannot be neglected for low capillary
78 porosities where gel pores form dominant pathway. Due to the hierarchical pore
79 structure and complex surface chemical properties of C-S-H [26-28], to study the

mechanism of species diffusion in cement paste is difficult. To overcome these difficulties, the previous efforts have been taken to understand the species diffusion in C-S-H at separate scales [29-33]. At molecular scale, to quantitatively analyze the influence from surface on species diffusion, Zhou et al. [33, 34] calculated the species density distribution and mobility near the surface of C-S-H by the molecular dynamics simulation. They found that the negative charged surface caused the aggregation of calcium ions and this physical bounding effect can slow down the mobility of species. However, in terms of computation cost it is rather difficult to conduct molecular modeling simulations to investigate species diffusion in the hierarchical pore structure of C-S-H. At continuum scale, Zhang et al. [31] recently presented a multiscale pore-network approach to analyze the correlation of surface EDL with hierarchical gel pore network on the ion diffusion. Through their simulations, they demonstrated that the surface EDL effect on ion diffusivity is sensitive to pore size. However, in their modeling approach the Stern layer was considered to be non-diffusive which would result in lower diffusivity values as compared to both molecular simulations [32, 33] and experimental results [30]. This indicates that ions might be mobile in stern layer and surface steric effect slows the diffusion in the pores. One should note that the thickness of the Stern layer in C-S-H varies from 0.6 nm to 0.8 nm [31], which is significant when compared to the gel pore size. Therefore, the contribution from the Stern layer should be accounted for the transport phenomena is C-S-H phase. However, the continuum-scale modeling is difficult to deal with the ion distribution in the Stern

layer.

To provide better understanding of ion transport through multi-scale cement paste microstructure and to account for double layer effects, in this study, a multiscale modeling is proposed which combines the pore-scale modeling with the atomic-scale modeling. The multiscale approach employed in this study is depicted schematically in Fig. 3. At C-S-H scale, ion transport is modelled using pore-scale lattice Boltzmann method-based solver. Using pore-scale solver we solve a set of modified Poisson-Nernst-Planck (PNP) equations to correctly account steric effects and to provide the correction of ion concentration near surface. The modified PNP model uses the concentration and electrical potential obtained from the molecular-scale Grand Canonical Monte Carlo simulations to compute excess chemical potential which corrects the concentration profiles obtained from classical PNP model. Finally, the C-S-H diffusivity obtained is utilized to predict diffusivity of ions in cement paste. Details on multiscale framework for ion transport are presented in section 2. Following that, we validate the formulation for modified PNP model by comparing with the molecular simulations. Using the modified PNP model Section 3.1 elucidates the relationship between effective diffusivities of charged and uncharged species with pore size in a simple channel. Finally, in section 3.2 results on calculation of the effective diffusivity in virtual microstructure of C-S-H phase and cement-paste are discussed.

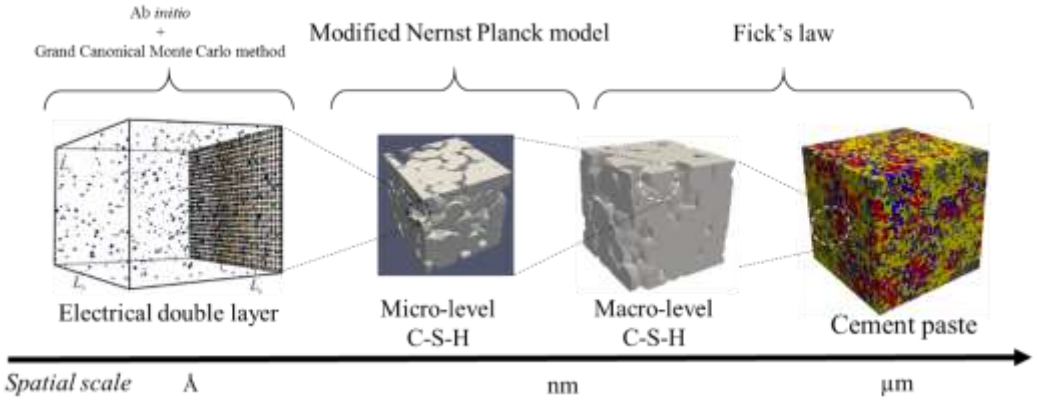

Fig. 3 Multi-scale representation of the cement paste structure and the multiscale modeling approach. The molecular-level information is used to correct ion distribution within the electrical double layer. The species diffusion at each scale is calculated by using the molecular simulation, the modified Nernst Planck model and the Fick's law, respectively (left to right).

2. Multiscale modeling

2.1. Numerical regeneration of hierarchical pore structure of cement paste

The microstructure of cement paste exhibits a complex hierarchical structure, in which pore size ranges from nanometers to micrometers [35-37]. In the past three decades, different microstructure characterization techniques such as scanning electron microscope, computer homographs, neutron scattering and NMR analysis as well as simulations have been employed to understand and represent the microstructure of cement paste and utilize this microstructure to obtain corresponding mechanical, chemical or physical properties [26, 38-41]. Since the properties of cement paste are sensitive to the surrounding chemical and physical environment, direct experimental measurements are difficult and it is easy to alter or even destroy the natural texture. Mesoscopic modeling approaches are often used to reconstruct the cement paste texture

based on the observations and atomistic simulations [26, 35, 38, 42-45].

To have consistent representation of microstructures of cement paste from nano- to micro-scale we have utilized the description provided by Bentz et al. [42]. Bentz et al. [42] represented the nanoscale C-S-H structure to have two level of self-similar structures: micro- and macro-level. In each level, an assembly of cluster of C-S-H particles is presented by the soft spheres controlled by the hard-core-soft-shell representation. At microscale, the voxel-based CEMHYD3D model (available in VCCTL software [46]) is used in this study to generate the virtual microstructures of cement paste. It should be noted that different descriptions have been proposed both at nano- and micro-scale. For nano-scale improved colloidal models [28, 40, 43], disk based packing models [47] and sheet based models [45] for C-S-H has been proposed. Despite these advancements, the nanoscale pore-network of C-S-H is still unknown as it is not yet possible to experimentally capture the image of C-S-H structures down to the nano-scale. Similarly, at micro-scale different microstructure generation and hydration models apart from CEMHYD3D exists such as HYMOSTRUC [48], μic [49] and HydratiCA [50]. However, the correct representation of cement paste microstructure is still under debate and widely researched. Therefore, in this study we have employed Bentz et al. approach due to its consistency in description of nano- and micro-structure. It has been widely recognized and has been successful in explaining different experimental observations.

2.2. Modeling ion diffusion in C-S-H

2.2.1. Monte Carlo method

The estimation of ion distribution in Stern layer is not straightforward. Several theoretical models have been developed to capture ion distribution in stern layer [51-55]. However, the applicability of these theoretical models for cementitious material is still not proven. Hence, in this study we utilize experimentally validated Grand Canonical Monte Carlo (GCMC) simulation of ion uptake C-S-H using the primitive model of electrolyte to obtain ion distribution in stern layer [56]. The GCMC simulation can be viewed as one-dimensional setup, which provides equilibrium concentration and potential distribution profiles near C-S-H surface. The simulation domain for GCMC consists of a box with C-S-H surface at one end as shown in Fig. 1. The surface charged density of C-S-H surface depends on the *p*H value and is calculated from the ab initio simulations which indicate that the surface of C-S-H can be represented by titrating surface sites >SiOH with the site density 2.4 sites/nm^2. The sites are distributed in pairs according to the crystal structure of tobermorite. The solvent of the pore solution is approximated by a dielectric continuum with the permittivity $\varepsilon = \varepsilon_r \varepsilon_0 = 6.95\times10^{-10}\ \mathrm{C^2/J\cdot m}$. The ions in the solution are represented by hard spheres with the same radius 0.2 nm.

The Monte Carlo simulation provides equilibrium concentration profiles of ions $C_i^{GCMC}(\mathrm{x})$. The mean electrostatic potential at the distance *x* to the surface is obtained by integrating the charge density distribution $\rho_e(\mathrm{x}) = \sum_i z_i C_i^{GCMC}(\mathrm{x})$:

$$\psi^{GCMC}(x) = -\frac{1}{\varepsilon_r \varepsilon_0}\int_x^{\infty}(t-x)\rho_e(t)\,\mathrm{d}t\,. \tag{1}$$

Note that above equation is obtained by integration of the Poisson equation. Finally, this molecular simulation presents the one-dimensional concentration and potential distributions away from the C-S-H surface in each situation.

2.2.2. Governing equations for ion transport at pore-scale

- **Ion transport in micro-level C-S-H**

Ion transport at the pore scale in the micro-level C-S-H can be described using the Poisson-Nernst-Planck (PNP) equations [24, 57] given as:

$$\frac{\partial C_i}{\partial t} + \nabla \cdot \boldsymbol{J}_i = 0\,, \tag{2}$$

$$\boldsymbol{J}_i = -D_{i,0}\nabla C_i - D_{i,0}\frac{z_i e C_i}{kT}\nabla \psi\,, \tag{3}$$

where C_i, $D_{i,0}$, $\boldsymbol{J}_i$ and z_i denotes the aqueous concentration (mol/m^3), diffusion coefficient in free water (m^2/s), flux (mol/m^2/s) and valence of the i^{th} species, respectively. t is time (s), e the absolute charge of electron (C), k the Boltzmann constant (J/K) and T the absolute temperature (K). In the above equation the local electrical potential ψ (V) is obtained from the following Poisson equation:

$$\nabla^2\psi = -\frac{\rho_e}{\varepsilon_r\varepsilon_0} = -\sum_i \frac{N_A e z_i C_i}{\varepsilon_r \varepsilon_0}\,, \tag{4}$$

where ρ_e is the net charge density (C/m^3) and N_A the Avogadro's number (mol^{-1}). Equations (3) and (4) are derived under the assumption that ions in electrolyte are considered as charge points ignoring their volumetric effects. Therefore, equations (3) and (4) are valid only under dilute conditions [58]. In order to account for steric effects,

the modification to classical PNP model is proposed. To derive the modified PNP model it is assumed that since the charge balance within EDL is extremely rapid [59] and the ion near C-S-H surface is in chemical quasi-equilibrium state. Under this condition, the chemical potential must be equal in the Stern layer, diffuse layer and bulk solution [53]:

$$kT\ln\left(a_{i,\infty}\right)=kT\ln\left(a_i\left(x\right)\right)+z_i e\psi\left(x\right)+\hat{\mu}_i^{ex}, \tag{5}$$

where $a_{i,\infty}$ and a_i are the activity of i^{th} species in the bulk solution and EDL, respectively. In equation (5), an excess term $\hat{\mu}_i^{ex}$ is added to the classical chemical potential, caused by the steric effect and ion-ion correlation. Considering $a_i=\gamma_i C_i$, we have:

$$\begin{aligned} kT\ln\left(C_{i,\infty}\right)&=kT\ln\left(C_i\left(x\right)\right)+z_i e\psi\left(x\right)+\left(\hat{\mu}_i^{ex}+kT\ln\left(\frac{\gamma_i\left(x\right)}{\gamma_{i,\infty}}\right)\right). \\ &=kT\ln\left(C_i\left(x\right)\right)+z_i e\psi\left(x\right)+\mu_i^{ex} \end{aligned} \tag{6}$$

This excess chemical potential μ_i^{ex} should be near zero within diffuse layer or free water. The flux in the Nernst-Planck equation is modified as follows:

$$\boldsymbol{J}_i=-D_{i,0}\nabla C_i-D_{i,0}\frac{z_i eC_i}{kT}\nabla\psi-D_{i,0}\frac{C_i}{kT}\nabla\mu_i^{ex}. \tag{7}$$

The boundary condition for ion diffusion on the solid-liquid interface is the non-flux boundary condition and for potential is the constant electrical potential (Dirichlet boundary condition).

According to equations (5), the concentration with respect to the distance *x* away from charged surface follows:

$$\frac{C_i\left(x\right)}{C_{i,\infty}}=\exp\left(-\frac{ez_i}{kT}\psi\left(x\right)-\frac{1}{kT}\mu_i^{ex}\left(x\right)\right), \tag{8}$$

and therefore, the dimensionless excess chemical potential μ_i^{ex}/kT in the Stern layer along the direction perpendicular to surface of C-S-H is given by:

$$\frac{1}{kT}\mu_i^{ex}(x) = -\frac{ez_i}{kT}\psi^{GCMC}(x) - \ln\left(\frac{C_i^{GCMC}(x)}{C_{i,\infty}}\right). \tag{9}$$

Substituting the distributions $C_i^{GCMC}(x)$ and $\psi^{GCMC}(x)$ obtained from the Grand Canonical Monte Carlo method into equation (9) we get the distribution of μ_i^{ex}/kT in the Stern layer, which is then fitted with a nonlinear function $F(x, C_{i,\infty})$ to get the relationship of μ_i^{ex}/kT with respect to the distance *x* and bulk concentration $C_{i,\infty}$ as:

$$\mu_i^{ex}(x, C_{i,\infty})/kT = F(x, C_{i,\infty}). \tag{10}$$

The effective diffusivity in the micro-level C-S-H is calculated by [24]:

$$D_{i,e}^{\text{Micro}} = \frac{\int J_i \mathrm{d}S}{S} \cdot \frac{L}{\Delta C_i}, \tag{11}$$

where $\int J_i \mathrm{d}S / S$ is the species flux per unit cross-section in the steady state, L the medium length and ΔC_i the mean concentration difference between two sides of the medium.

- **Ion transport in macro-level C-S-H and cement paste**

Since the mean pore size of macro-level C-S-H is large enough, the electrokinetic effect can be ignored. The $D_{i,e}^{\text{Micro}}$ is as input as the diffusion coefficient of solid phase in macro-level C-S-H to get the effective diffusivities in macro-level C-S-H $D_{i,e}^{\text{Macro}}$ by the Fick's law:

$$\boldsymbol{J}_i = -D_{k,0}\nabla C_i, \tag{12}$$

$$D_{k,0} = \begin{cases} D_{i,0}, & \text{Pore} \\ D_{i,e}^{\text{Micro}}, & \text{Solid} \end{cases}. \tag{13}$$

The effective diffusivity in the macro-level C-S-H is:

$$D_{i,e}^{\text{Macro}} = \frac{\int J_i \mathrm{d}S}{S} \cdot \frac{L}{\Delta C_i}. \tag{14}$$

2.2.3. Lattice Boltzmann method

Lattice Boltzmann (LB) method has shown good performances for simulating fluid flow [60, 61] and modeling multi-physical transports in porous media with complex geometries [62-64]. Benefiting its advantages for modeling transport processes in porous media, the modified Poisson-Nernst-Planck equations described in section 2.2.2 are solved using LB method. The LB solver has been optimized and implemented to run on Tesla-K80 GPGPU to provide additional speed up compared to its CPU implementation allowing use to handle large computational domains.

In this study, the SRT collision operator (with maximum value of relaxation parameter equal to one) is employed. Chai et al. [65] indicated that for relaxation time less than or equal to one the difference between SRT and MRT schemes for computing diffusion coefficient is less than 1%. Hence, SRT scheme has been chosen as it is computationally more efficient than MRT. Secondly, we choose consistent D3Q7 lattice for both diffusion and electro-kinetic potential evolution since for these processes this model is proven to be very stable and robust [24]. Moreover, it is more efficient compared to higher order lattice schemes. In the LB framework, the state of the system is evolved in terms of distribution function which corresponds to concentration C_i and potential ψ

are [24]:

$$f_{i,\alpha}\left(\boldsymbol{r}+c_{f_i}\delta t_{f_i}\boldsymbol{e}_\alpha,t+\delta t_{f_i}\right)-f_{i,\alpha}\left(\boldsymbol{r},t\right)=-\frac{1}{\tau_{f_i}}\left[f_{i,\alpha}\left(\boldsymbol{r},t\right)-f_{i,\alpha}^{eq}\left(\boldsymbol{r},t\right)\right], \quad (15)$$

$$h_\alpha\left(\boldsymbol{r}+c_h\delta t_h\boldsymbol{e}_\alpha,t+\delta t_h\right)-h_\alpha\left(\boldsymbol{r},t\right)=-\frac{1}{\tau_h}\left[h_\alpha\left(\boldsymbol{r},t\right)-h_\alpha^{eq}\left(\boldsymbol{r},t\right)\right]+\omega_\alpha\delta t_h\frac{\rho_e}{\varepsilon_r\varepsilon_0}, \quad (16)$$

where $f_{i,\alpha}$ and h_α denote the distribution functions for concentration of i^{th} ion and electrical potential, respectively. The equilibrium distribution functions are:

$$f_{i,\alpha}^{eq}=\omega_\alpha C_i\left[1-\frac{4D_{i,0}}{kT}\frac{\boldsymbol{e}_\alpha\left(ez_i\nabla\psi+\nabla\mu_i^{ex}\right)}{c_{f_i}}\right], \quad (17)$$

$$h_\alpha^{eq}=\omega_\alpha\psi, \quad (18)$$

where $c_{f_i}=\delta x/\delta t_{f_i}$. δx is the lattice size and δt_{f_i} the lattice time for i^{th} ion diffusion. In D3Q7 model the distribution coefficients $\omega_\alpha=1/4$ for $\alpha=0$ and $\omega_\alpha=1/8$ for $\alpha=1\sim6$. The discrete velocities $\boldsymbol{e}_\alpha$ of D3Q7 lattice are are:

$$\boldsymbol{e}_\alpha=\begin{cases}(0,0,0) & \alpha=0\\ (\pm1,0,0),(0,\pm1,0),(0,0,\pm1) & \alpha=1-6\end{cases}. \quad (19)$$

The relaxation time for ion diffusion is related to the diffusion coefficient in free water by $\tau_{f_i}=4D_{i,0}\delta t_{f_i}/\delta x^2+0.5$ and the relaxation time for the potential is $\tau_h=4\delta t_h/\delta x^2+0.5$. The local concentration and potential are obtained from distribution functions using $C_i=\sum f_{i,\alpha}$ and $\psi=\sum h_\alpha$. It can be shown that the above conditions, the evolution equations can recover the governing equations (2), (4) and (7) using the Chapman-Enskog expansion. In the LB scheme the gradient of potential can be determined by the local potential distribution functions [66] and the gradient of excess potential is calculated by the difference method. The corresponding

numerical boundary conditions are the same as mentioned in [24]: the zero normal flux boundary condition using 'bounce-back' scheme as $f_{i,\alpha}\left(\boldsymbol{r},t+\delta t_{f_i}\right)=f_{i,\beta}\left(\boldsymbol{r},t\right)$, the constant concentration boundary condition through $f_{i,\alpha}\left(\boldsymbol{r},t+\delta t_{f_i}\right)=-f_{i,\beta}\left(\boldsymbol{r},t\right)+0.25C_{i,\infty}$ and constant potential boundary condition using $g_{\alpha}\left(\boldsymbol{r},t+\delta t_{g}\right)=-g_{\beta}\left(\boldsymbol{r},t\right)+0.25\psi_{d}$, where the index α and β are the opposite directions normal to the interface.

2.3. Calibration

In this section, the modified PNP formulation is compared with the results obtained from the GCMC simulations in order to demonstrate the use of excess potential provides correct concentration profiles in stern layer. Additionally, comparison of modified PNP is also made with classical PNP model to emphasis the need of modified PNP to correctly capture ion concentrations near surface. The simulation domain consist of the C-S-H surface at one end in contact with the pore solution consisting of $Ca(OH)_2$ electrolyte. The GCMC simulation setup consists of a three dimensional $40\ \text{nm}\times 40\ \text{nm}\times 40\ \text{nm}$ cubic domain. The temperature is set to 298.15 K and the absolute permittivity of the medium is set to $6.95\times10^{-10}\ \text{C}^2/\text{J}\cdot\text{m}$. The dimensionless excess chemical potential computed using Eq. (9) as a function of distance *x* obtained from GCMC is shown in Fig. 4. For lattice Boltzmann method we use a one-dimensional domain, with length equal 100 nm and lattice spacing equal to 0.02 nm. For modified PNP model the surface electrical potential ψ_0 is used as the boundary condition at the surface. The surface electrical potential is a function of the *p*H and is

given as $\psi_0 = -0.0226pH + 0.0822$ (V) which is obtained from GCMC simulation. Zeta potential (ψ_d) equals to 20 mV [31] used as boundary condition near the surface for classical PNP model. Zeta potential is defined at the location of the slipping plane near the interface between the Stern layer and the diffuse layer and in this study the position of slipping plane is assigned to be one and a half ion diameter (0.6 nm) from the surface. The equilibrium potential and ion distributions with respect to the distance away from C-S-H surface obtained from classical PNP model and the modified PNP model are plotted in Fig. 5. It is clear that near the surface classical PNP model significantly over predicts the ion concentration for both calcium and hydroxyl ions compared to the modified model and GCMC simulations.

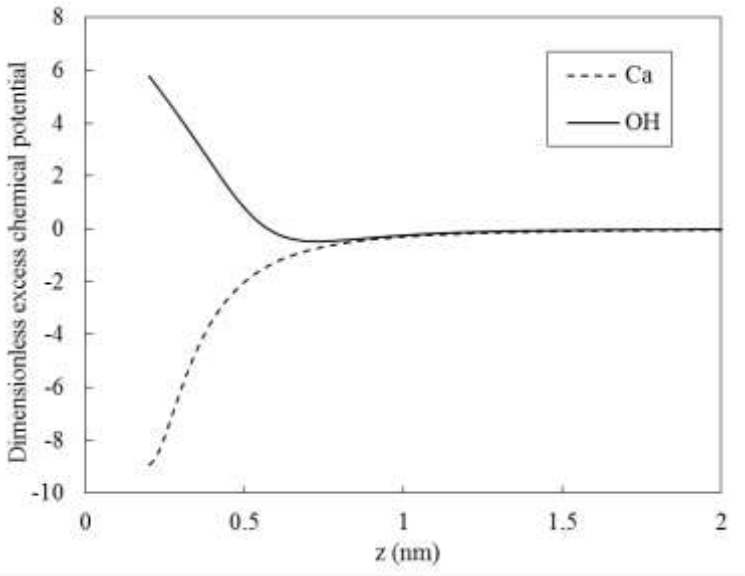

Fig. 4 The dimensionless excess chemical potential μ_i^{ex}/kT obtained by the Monte Carlo simulation as a function of distance away from C-S-H surface. The dashed line is the calcium ion and the solid hydroxyl ion. The charged surface is set at z = 0 and as far away from surface the value of μ_i^{ex}/kT is near zero. The pH is 12.5 and the bulk concentration of $Ca(OH)_2$ is 20 mol/m^3.

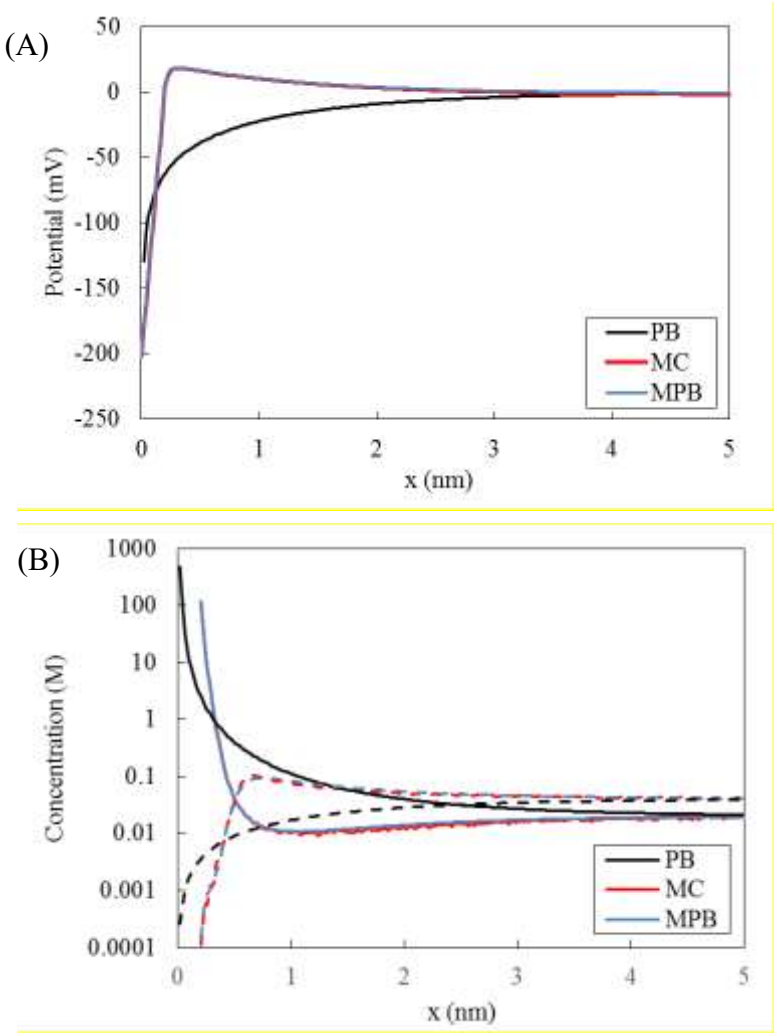

Fig. 5 The electrical potential (A) and ion concentration distribution (B) with respect to the distance *x* normal to the C-S-H surface. The red lines are from the Monte Carlo simulation from [56], blue lines modified PNP model (MPB) and black lines classical PNP model (PB). In figure (B), the dash line denotes hydroxide ion and solid calcium ion. In C-S-H, the thickness of Stern layer for classical PNP model is set as 0.6 nm [56].

3. Results and discussion

In this section the proposed multiscale modeling approach has been utilized to first obtain effective diffusion of charged species in a single C-S-H pore to investigate systematically the effect of pore-size on effective diffusivity. Later the model is applied to obtain the effective diffusivity from hierarchical C-S-H structure and cement paste

microstructure. The pore solution in simulation is simplified as a mixture of $Ca(OH)_2$ and NaCl with *p*H =12.5 and the temperature set to 298.15 K. Due to the constant *p*H and temperature, the surface of C-S-H is assumed to be homogeneous charged. Results obtained from modified PNP equation are also compared with classical PNP model to highlight the impact of stern layer on effective diffusivity which has been considered to be non-diffusive in previous studies [20, 24, 31]. For the classical PNP model, the Stern layer is assumed to be immobile, and zeta potential is set as 20 mV as mentioned before. The stern layer thickness is assumed to be 1.5 layers of hydrated ion which is equal to 0.6 nm. The first layer of hydrated ions in stern layer consist of calcium ion which has very low mobility due to strong bonding of bivalent ion to the surface as reported in literature based on molecular dynamic simulations[67-69]. Therefore, for modified PNP model the first adsorbed layer of Stern layer is considered non-diffusive. However, the ions in the second adsorbed layer are mobile in case of modified PNP model. For simplification same diffusion coefficient $1\times10^{-9}\ m^2/s$ is used for all species in free water.

3.1. Diffusivity in single pore

The simulation domain for single pore consists of a two-dimensional straight channel with two reservoirs as shown in Fig. 6. The width of channel *w* is changed from 1.0 nm to 20 nm to mimic different pore size and porosity of the system is kept equal to 0.5 by maintaining constant ratio for channel width to vertical domain width *w/H* as 0.5. The

lattice spacing is set to 0.1 nm. The surface electrical potential is set to -0.205 V corresponding to pH equal to 12.5. For the inlet/outlet boundary conditions, we set a zero electrical potential and fixed concentration for each ion. For all other directions periodic boundary conditions are applied. The concentration of $Ca(OH)_2$ at inlet and outlet is set to the same value of 20 mol/m^3. The concentration of HTO at inlet is set as 20.5 mol/m^3 and 19.5 mol/m^3 at outlet. Two mean concentrations of NaCl (10 mol/m^3 and 100 mol/m^3) are adopted to investigate how the NaCl concentrations affect the effective diffusion coefficient, and the normalized concentration difference $\left(C_{\text{inlet},i} - C_{\text{inlet},i}\right)/C_i$ is equal to 0.1. The values of concentration boundary conditions of NaCl at inlet and outlet are listed in Table 1.

Table 1 Concentration boundary conditions of NaCl at inlet and outlet for simulation

	Mean concentration	
	10 mol/m^3	100 mol/m^3
Inlet concentration (mol/m^3)	10.5	105
Outlet concentration (mol/m^3)	9.5	95

The normalized effective diffusivity with respect to the pore size shows a complex nonlinear relationship as shown in Fig. 7. For instance, the normalized effective diffusivity of chloride ion reaches the peak as the channel width is 2 nm and quickly drops below this width. The normalized effective diffusivities of HTO and sodium, in contrast, always decrease when the channel width is reduced. For channel widths larger

than 1.2 nm the effective diffusivity of chloride is larger than for sodium and HTO. However, for small pores (<=1.2 nm), since the Stern layer mainly occupies the pore space it is difficult for negative charged species to access the pores, and therefore, HTO effective diffusivity is higher than that of chloride ion. To quantify the applicability of classical PNP model for each species, it assumed that when the relative difference between classical PNP model and modified PNP model is less than 20% it is considered to be valid. For chloride and HTO the classical PNP model is found to be valid for pore size larger than 3 nm. However, due to the complex electrical adsorption (physical adsorption) of sodium ion in the Stern layer the classical PNP model is only valid for pore size lager than 20 nm. The surface of C-S-H is negative charged and the concentration of chloride ions are higher than sodium ions in diffuse layer due to the charge reversal (shown in Fig. 1). This is the main reason why the effective diffusivity of chloride ion is larger than that of sodium ion. As a result, when the channel width is less than 3 nm, the contribution form Stern layer cannot be ignored and the classical PNP model will underestimate the effective diffusivity. For channel widths larger than 20 nm the EDL effect vanishes for all species. Fig. 9 shows the effective diffusion coefficients calculated by the modified PNP model with NaCl concentration of 10 mol/m^3 and 100 mol/m^3. Due to the constant *p*H value of pore solution, the surface charge density is constant for both concentrations. As the surface charge in C-S-H is mainly balanced by the calcium ions, the sodium ion does not significantly alter the thickness of EDL. Therefore, although the concentration of NaCl changes one order the

effective diffusion coefficients in C-S-H of sodium and chloride ions hardly varies.

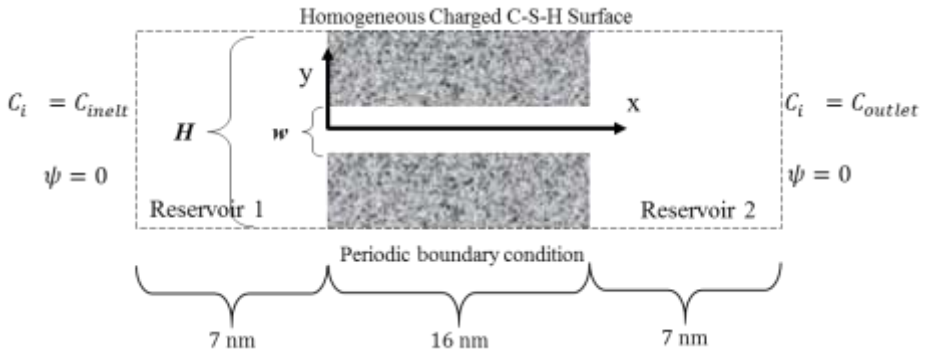

Fig. 6 The simulation domain of simple two-dimensional channel and corresponding boundary conditions. The width of channel *w* changes from 1 nm to 20 nm and *w/H* is constant as 0.5.

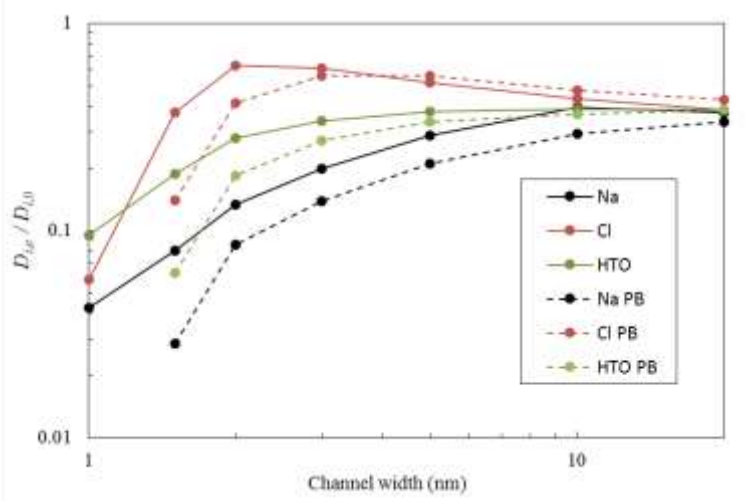

Fig. 7 Normalized effective diffusion coefficients of Na^+, Cl^- and HTO with respect to widths of channel. The solid lines are calculated by our modified PNP model and dash lines are from classical PNP model (PB). Red denotes chloride ion, green HTO and black sodium ion. NaCl concentration is 10 mol/m^3 and $Ca(OH)_2$ 20 mol/m^3.

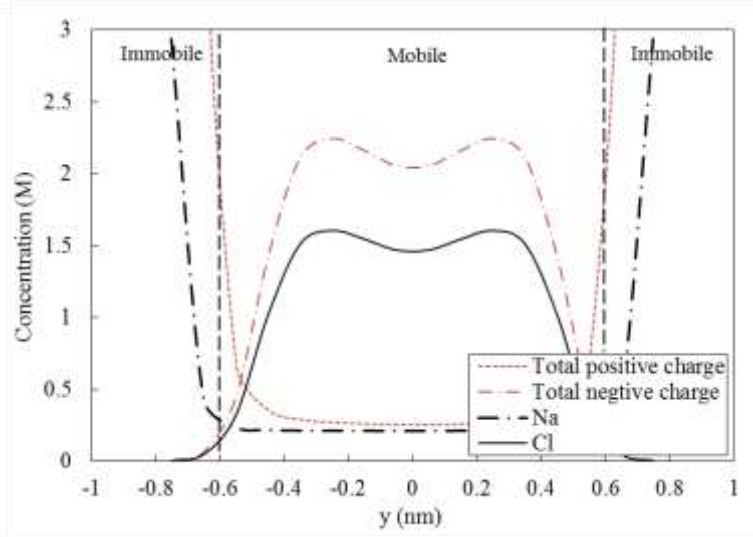

Fig. 8 The concentration distribution of middle cross section in 2D channel by the present simulation. The width of channel is 2 nm. The charged C-S-H surface is in ±1 nm and the first-adsorbed layer is immobile.

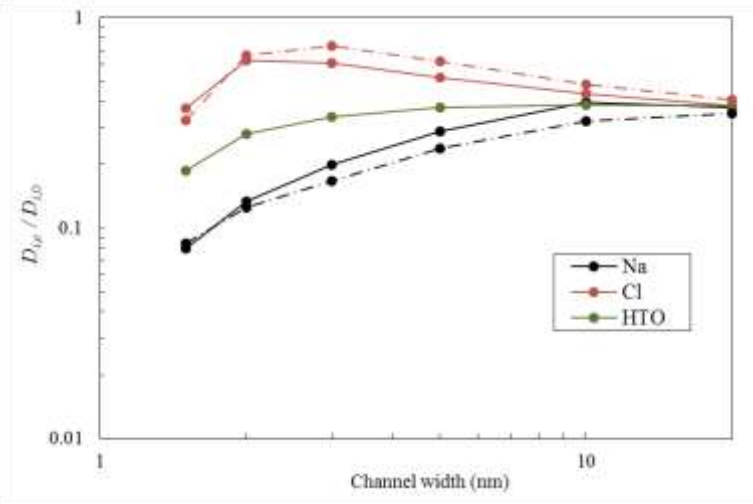

Fig. 9 Normalized effective diffusion coefficients of Na^+, Cl^- and HTO with respect to ion concentration. We use two concentrations of NaCl 100 mol/m^3 and 10 mol/m^3 but the same concentration 20 mol/m^3 for $Ca(OH)_2$. The solid lines are calculated by using 100 mol/m^3 NaCl and dash-point lines 10 mol/m^3 NaCl. Red denotes chloride ion, green HTO and black sodium ion.

3.2. Effective diffusivity from virtual cement microstructures

In this section, in order to compare modeling results with the experiment data shown in Fig. 2 the effective diffusion coefficients in C-S-H $D_{i,e}^{\text{C-S-H}}$ are first calculated in section

3.2.1 and $D_{i,e}^{\text{C-S-H}}$ are then used to predict the effective diffusivities in cement paste in section 3.2.2.

3.2.1. Effective diffusivity in C-S-H phase

For the micro-level C-S-H structures, the solid is non-diffuse and the surface is homogeneous charged. The surface electrical potential is -0.21 V at pH=12.5. However, in macro-level C-S-H structures, the solid phase is diffusive and the diffusion coefficient of the solid phase is set to the one obtained from micro-level C-S-H structure by changing the relaxation time in LB scheme.

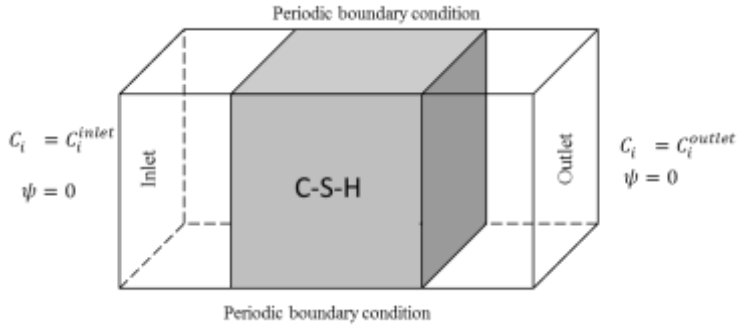

Fig. 10 The simulation domain of C-S-H phase and corresponding boundary conditions.

For the regenerated micro-level C-S-H structure, the porosity is 22.3% and the mean pore size is 1.59 nm computed by the maximum sphere algorithm [70]. Within these narrow pores EDL effects cannot be ignored and the classical PNP model is not valid. Therefore, the modified PNP model proposed in this study has been used to calculate the effective diffusivity $D_{i,e}^{\text{Micro}}$ in the regenerated micro-level C-S-H microstructures. The size of the three-dimensional simulation domain is 32.5 nm × 25 nm × 25 nm

meshed by a uniform 260×200×200 grid. The boundary conditions are shown in Fig. 10 and the average concentrations of $Ca(OH)_2$ and NaCl are 20 mM and 10mM, respectively. Fig. 11 shows micro-level C-S-H pore space generated for the three-dimensional simulations and the corresponding steady-state chloride ion concentration distribution in the pore space. The effective diffusivity in the macro-level C-S-H is calculated by the Fick's law. The simulation domain of macro-level C-S-H is 325 nm × 250 nm × 250 nm with the lattice spacing equal to 1.25 nm. The normalized effective diffusion coefficients are shown in Table 2.

(A)

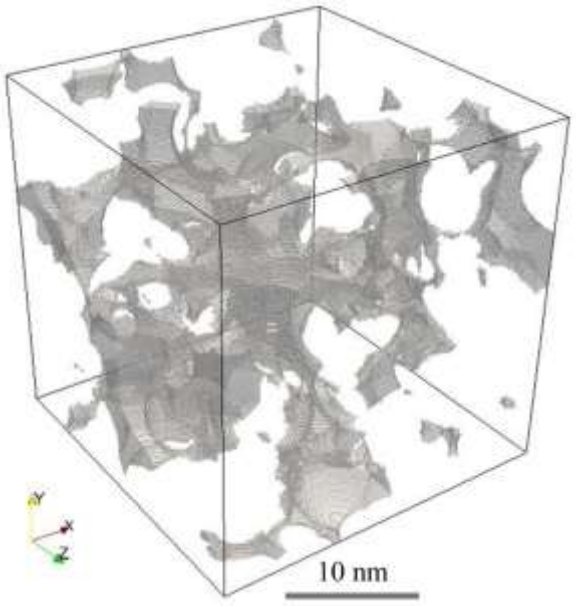

(B)

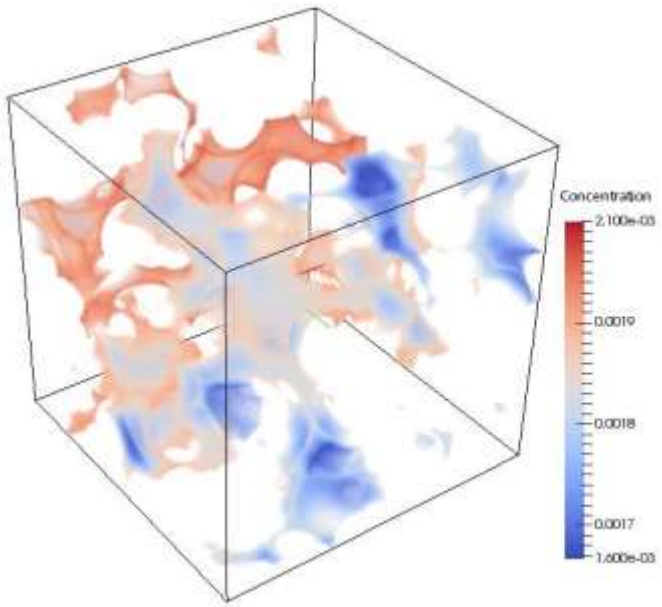

Fig. 11 (A) Visualization of gel pores regenerated by the Bentz et al. method [42] and (B) the steady distribution of chloride ion concentration in micro-level C-S-H are shown. The solid phase is hyaline and invisible. Stochastic characteristics are very clear for the ion concentration across one section.

Table 2 Normalized effective diffusion coefficients of Na^+, Cl^- and HTO in micro- and macro-level C-S-H

Normalized Effective diffusivity*	Na^+	Cl^-	HTO
Micro-level C-S-H $D_{i,e}^{\text{Micro}} / D_{i,0}$	0.00871	0.0259	0.0244
Macro-level C-S-H $D_{i,e}^{\text{Macro}} / D_{i,0}$	0.0244	0.0455	0.0438

* The effective diffusivities are normalized by the diffusion coefficients in the free water $D_{i,0}$.

3.2.2. Effective diffusivity in cement paste

The virtual microstructures of cement paste are obtained using CEMHYD3D (available in VCCTL software). The standard cement material “cement 140” from the VCCTL material library is used and the detail of component is shown Table 3. The water-cement ratios is set as 0.2, 0.3, 0.4 and 0.5, as hydration time equals to 7, 28 and 96 days. The

other parameters are kept as the default setting in VCCTL. The 100 µm × 100 µm × 100 µm virtual microstructures of cement paste are used as the simulation domain, which is discretized using a 100 × 100 × 100 uniform regular grid. The size of simulation domain chosen here is sufficient to have a representative elementary volume (REV) as proven through numerical studies [2, 71, 72] and experimentally through image technique [73]. The concentration 2.0 mol/m^3 is employed as the boundary conditions at inlet and 1.0 mol/m^3 at outlet [24]. The virtual cement paste microstructures have three type phases: capillary pores, C-S-H phase and other solid phases. Other solid phases include hydration phases other than C-S-H and unhydrated clinkers which are treated as non-diffusive. Ion diffusivity in capillary pores is assumed to be identical to diffusivity in free water.

Table 3 The major phase volume fractions of "cement 140" in VCCTL used in study.

C_3S	C_2S	C_3A	C_4AF
0.6576	0.180	0.0994	0.0633

Simulations in previous sections have been carried out under the assumption that the local mobility of each species in the C-S-H is the same as in the free water. However due to the electro viscosity and steric effects near the surface, the molecular dynamic simulations [32, 34, 74, 75] has shown that the ions in gel pores of C-S-H has only 25% -50% percent mobility than that in the free water. The quasi-elastic neutron scattering

(QENS) experiments [30] also suggested that the water in gel pores diffuses slowly ($\sim 10^{-10}$ $m^2 s^{-1}$). Moreover, the colloidal representation of C-S-H developed by Bentz [42] may not give correct pore size distribution and as a result the model connectivity might be much higher than that of the real C-S-H structures. Therefore, in this study, the effective diffusivity in C-S-H $D_{i,e}^{\text{C-S-H}}$ is determined by:

$$D_{i,e}^{\text{C-S-H}} = D_{i,e}^{\text{Macro}} / \delta_D , \tag{20}$$

where δ_D is the attenuation factor to indicate slow-down degree of mobility in gel pores of C-S-H. The effective diffusivities of species in cement paste are calculated by equation (14). A parametric study has been carried out to roughly identify the attenuation factor for ionic mobility within gel pores [30, 34] by varying it from 5 to 20 shown in Fig. 12. Fig. 12 compares the effective diffusivities obtained from simulations with experiment data presented in Fig. 2. If $\delta_D = 1$, the effective diffusivity computed is higher than the experimental values. The parametric study reveals that the value of the attenuation factor δ_D for chloride ion and HTO should be around 5~10 and for sodium ion around 20. It means that the local mobility in C-S-H has a significant influence on mass transport in confined nanopores of cement paste and the better representation of the C-S-H pore-structure is needed.

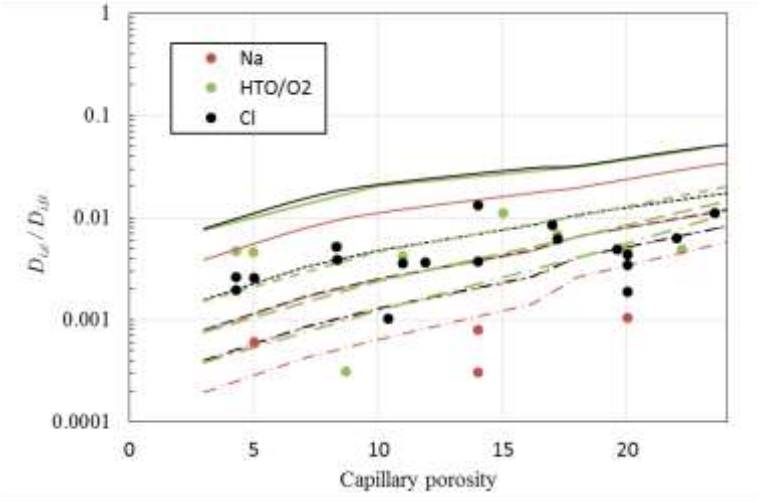

Fig. 12 Comparison of calculated and experimentally measured effective diffusion coefficients. Points are the diffusion coefficients by experimental measurement collected from references [4-17] (see detail in Appendix) and solid lines are from our simulations by using the attenuation factor $\delta_D = 1$; dotted lines are $\delta_D = 5$; dashed lines $\delta_D = 10$; dotted-dashed lines $\delta_D = 20$.

4. Conclusions

The goal of this study was to quantify the charged or non-charged transport in cement paste microstructure accounting for EDL effects near charged C-S-H surface. To achieve this goal a multiscale modeling framework has been presented which combines Grand canonical Monte Carlo simulation at molecular scale with the lattice Boltzmann method at pore scale. The proposed methodology is first applied to investigate effect of pore-size on species transport and later applied to obtain effective diffusivity of C-S-H. The C-S-H diffusivity obtained has been utilized as an input at cement paste scale to predict effective diffusivity in microstructures of cement paste. A coupling between pore scale modeling approach and molecular modeling approach can be successfully achieved using the proposed modified PNP model thus bridging the scale gap between

512 the two models. The effective diffusivity with respect to pore size shows a complex
513 nonlinear relationship. For a simple channel geometry, the classical PNP model
514 compares well with the modified PNP model for chloride ion and HTO as long as the
515 width of channel is larger than 3 nm. The classical PNP model is not applicable to
516 describes sodium ion diffusion for pore size smaller than 20 nm. When the pore-size is
517 smaller than 3 nm, the influence of steric and ion-ion correlation effects is important
518 and the classical PNP model significantly over predicts the concentrations near surfaces.
519 At pore size around 2 nm the effective diffusivity of chloride ions has the peak value,
520 whereas the normalized effective diffusivity of HTO and sodium ion increases with
521 increase in the pore size.
522 Simulations presented in this study shows that the effective diffusion coefficient of
523 chloride ion in C-S-H is similar to that of HTO, but much larger than the sodium ion.
524 At cement paste scale, our model qualitatively captures the effects of electrical double
525 layer on diffusivity as reported experimentally. We found that in order to match
526 experiment data the model needs to include attenuation factors of 5-20. We relate this
527 partially to the poor description of hierarchical pore structure of cement paste and
528 partially to the unknown local mobility within gel pores near surface which can be
529 quantified in future using molecular dynamic simulations.
530

Appendix

The relative effective diffusion coefficients of Na^+, Cl^-, Cs^+, dissolved O_2 and HTO in saturated CEM I cement paste with respect to the capillary porosity collected from different references.

Species	Normalized diffusivity $D_{i,e}/D_{i,0}$	Water/cement ratio	Hydrated time (days)	Degree of hydration‡	Porosity	Ref.
Chloride	0.00123	0.4	7	0.6	25*	[5]
	0.00270	0.4	7	0.6	25*	
	0.00344	0.4	28	0.7	20*	[4]
	0.0133	0.3	7	0.6	14*	
	0.00435	0.4	28	0.7	20*	[6]
	0.00369	0.35	28	0.7	14*	
	0.0111	0.4	28	0.7	23.5	
	0.00635	0.35	28	0.7	22	
	0.00403	0.4	7	0.6	26*	[8]
	0.00187	0.4	28	0.7	20*	[10]
	0.00354	0.35	56	0.76	11*	[12]
	0.00254	0.25	56	0.76	5*	
	0.00194	0.4	84	0.79	4.3	[13]
	0.00389	0.5	84	0.79	8.36	

	0.00620	0.6	84	0.79	17.18	
	0.0105	0.7	84	0.79	24.86	
	0.00475	0.4	28	0.7	20*	[10]
	0.00465	0.4	84	0.79	4.3	
Oxygen	0.00520	0.5	84	0.79	8.36	[13]
	0.00682	0.6	84	0.79	17.18	
	0.0108	0.7	84	0.79	24.86	
	0.00491	0.45	21	0.68	22.2	[9]
Tritiated	0.00420	0.35	56	0.76	11*	[12]
water	0.00455	0.35	56	0.76	5*	
	0.0110	0.35			15	[76]
	0.000188	0.4	7	0.6	25*	[5]
	0.000601	0.3	84	0.76	5*	
	0.00105	0.4	28	0.7	20*	
Sodium	0.000308	0.35	28	0.7	14*	[4]
	0.000789	0.3	7	0.6	14*	
	0.00105	0.4	7	0.6	26*	[8]
	0.00000073	0.2	7	0.6	3*	
Cesium	0.0000731	0.3	7	0.6	13*	[16]
	0.000487	0.4	7	0.6	25*	

0.001463	0.5	7	0.6	34*	
0.000112	0.4	28	0.7	20*	[6]
0.0000790	0.35	28	0.7	14	
0.000419	0.4	28	0.7	23.5	[7]
0.000253	0.35	28	0.7	22*	
0.000878	0.4	7	0.6	26*	[15]
0.000575	0.4	28	0.7	20*	[17]
0.00117	0.42	28	0.7	22*	[14]
0.00419	0.42	28	0.7	22*	
0.000536	0.35	56	0.76	11*	[12]
0.000375	0.25	56	0.76	5*	

* The porosity is predicted by the Power's model.

‡ The degree of hydration is taken as suggested by Hansen [77].

Acknowledgement

Y. Yang and M. Wang acknowledges financial support by the NSF grant of China (No.51766107). Y. Yang acknowledges the financial support by China Scholarship Council's (CSC) Chinese Government Graduate Student Overseas Study Program. R. Patel acknowledges funding received from the European Union's Horizon 2020 research and innovation programme under the Marie Sklodowska-Curie grant

544 agreement No 701647.

545

Reference

[1] E.J. Garboczi, D.P. Bentz, Modelling of the microstructure and transport properties of concrete, Construction and Building Materials 10(5) (1996) 293-300.

[2] R.A. Patel, J. Perko, D. Jacques, G. De Schutter, G. Ye, K. Van Bruegel, Effective diffusivity of cement pastes from virtual microstructures: Role of gel porosity and capillary pore percolation, Construction and Building Materials 165 (2018) 833-845.

[3] C. Labbez, A. Nonat, I. Pochard, B. Jonsson, Experimental and theoretical evidence of overcharging of calcium silicate hydrate, J. Colloid Interface Sci. 309(2) (2007) 303-7.

[4] S. Goto, D.M. Roy, Diffusion of ions through hardened cement pastes, Cem. Concr. Res. 11(5) (1981) 751-757.

[5] S. Chatterji, Transportation of ions through cement based materials. Part 3 experimental evidence for the basic equations and some important deductions, Cem. Concr. Res. 24(7) (1994) 1229-1236.

[6] A. Kumar, B. Roy, Retardation of Cs+ and Cl− diffusion using blended cement admixtures, J. Am. Ceram. Soc. 69(4) (1986) 356-360.

[7] A. Kumar, S. Komarneni, D.M. Roy, Diffusion of Cs+ and Cl− through sealing materials, Cem. Concr. Res. 17(1) (1987) 153-160.

[8] S. Chatterji, M. Kawamura, Electrical double layer, ion transport and reactions in hardened cement paste, Cem. Concr. Res. 22(5) (1992) 774-782.

[9] A. Delagrave, J. Marchand, M. Pigeon, Influence of Microstructure on the Tritiated Water Diffusivity of Mortars, Advanced Cement Based Materials 7(2) (1998) 60-65.

[10] M. Castellote, C. Alonso, C. Andrade, G.A. Chadbourn, C.L. Page, Oxygen and chloride diffusion in cement pastes as a validation of chloride diffusion coefficients obtained by steady-state migration tests, Cem. Concr. Res. 31(4) (2001) 621-625.

[11] J. Tits, A. Jakob, E. Wieland, P. Spieler, Diffusion of tritiated water and 22Na+ through non-degraded hardened cement pastes, J. Contam. Hydrol. 61(1-4) (2003) 45-62.

[12] H.M. Johnston, D.J. Wilmot, Sorption and diffusion studies in cementitious grouts, Waste Manage. 12(2–3) (1992) 289-297.

[13] V.T. Ngala, C.L. Page, L.J. Parrott, S.W. Yu, Diffusion in cementitious materials: II, further investigations of chloride and oxygen diffusion in well-cured OPC and OPC/30%PFA pastes, Cem. Concr. Res. 25(4) (1995) 819-826.

[14] K.G. Papadokostaki, A. Savidou, Study of leaching mechanisms of caesium ions incorporated in Ordinary Portland Cement, J. Hazard. Mater. 171(1-3) (2009) 1024-31.

[15] A. Atkinson, A.K. Nickerson, Diffusion and Sorption of Cesium, Strontium, and Iodine in Water-Saturated Cement, Nucl. Technol. 81(1) (1988) 100-113.

[16] A. Atkinson, A.K. Nickerson, The diffusion of ions through water-saturated cement, Journal of Materials Science 19(9) (1984) 3068-3078.

[17] M. Castellote, C. Andrade, C. Alonso, Characterization of transport of caesium,

586 strontium, cobalt and iron ions through concrete by steady-state migration and natural
587 diffusion tests, Advances in Cement Research 11(4) (1999) 161-168.
588 [18] J.S. Murday, R.M. Cotts, Self‐Diffusion in Liquids: H2O, D2O, and Na, The
589 Journal of Chemical Physics 53(12) (1970) 4724-4725.
590 [19] M. Flury, T.F. Gimmi, 6.2 Solute Diffusion, in: J.H. Dane, C.G. Topp (Eds.),
591 Methods of Soil Analysis: Part 4 Physical Methods, Soil Science Society of America,
592 Madison, WI, 2002, pp. 1323-1351.
593 [20] H. Friedmann, O. Amiri, A. Aït-Mokhtar, Physical modeling of the electrical
594 double layer effects on multispecies ions transport in cement-based materials, Cem.
595 Concr. Res. 38(12) (2008) 1394-1400.
596 [21] C. Labbez, B. Jönsson, I. Pochard, A. Nonat, B. Cabane, Surface Charge Density
597 and Electrokinetic Potential of Highly Charged Minerals: Experiments and Monte
598 Carlo Simulations on Calcium Silicate Hydrate, The Journal of Physical Chemistry B
599 110(18) (2006) 9219-9230.
600 [22] M.A. Glaus, S. Frick, R. Rossé, L.R.V. Loon, Comparative study of tracer diffusion
601 of HTO, 22Na+ and 36Cl− in compacted kaolinite, illite and montmorillonite, Geochim.
602 Cosmochim. Acta 74(7) (2010) 1999-2010.
603 [23] J.P. Korb, L. Monteilhet, P.J. McDonald, J. Mitchell, Microstructure and texture of
604 hydrated cement-based materials: A proton field cycling relaxometry approach, Cem.
605 Concr. Res. 37(3) (2007) 295-302.
606 [24] Y. Yang, M. Wang, Pore-scale modeling of chloride ion diffusion in cement
607 microstructures, Cem. Concr. Compos. 85 (2018) 92-104.
608 [25] C.A.J. Appelo, Solute transport solved with the Nernst-Planck equation for
609 concrete pores with ‘free’ water and a double layer, Cem. Concr. Res. 101 (2017) 102-
610 113.
611 [26] I.G. Richardson, The calcium silicate hydrates, Cem. Concr. Res. 38(2) (2008)
612 137-158.
613 [27] S. Papatzani, K. Paine, J. Calabria-Holley, A comprehensive review of the models
614 on the nanostructure of calcium silicate hydrates, Construction and Building Materials
615 74 (2015) 219-234.
616 [28] H.M. Jennings, Refinements to colloid model of C-S-H in cement: CM-II, Cem.
617 Concr. Res. 38(3) (2008) 275-289.
618 [29] E.J. Garboczi, D.P. Bentz, Computer simulation of the diffusivity of cement-based
619 materials, Journal of Materials Science 27(8) (1992) 2083-2092.
620 [30] H.N. Bordallo, L.P. Aldridge, A. Desmedt, Water Dynamics in Hardened Ordinary
621 Portland Cement Paste or Concrete: From Quasielastic Neutron Scattering, The Journal
622 of Physical Chemistry B 110(36) (2006) 17966-17976.
623 [31] Y. Zhang, C. Liu, Z. Liu, G. Liu, L. Yang, Modelling of diffusion behavior of ions
624 in low-density and high-density calcium silicate hydrate, Construction and Building
625 Materials 155 (2017) 965-980.
626 [32] D. Hou, Z. Li, Molecular Dynamics Study of Water and Ions Transported during
627 the Nanopore Calcium Silicate Phase: Case Study of Jennite, J. Mater. Civ. Eng. 26(5)

628 (2014) 930-940.
629 [33] Y. Zhou, D. Hou, J. Jiang, L. Liu, W. She, J. Yu, Experimental and molecular
630 dynamics studies on the transport and adsorption of chloride ions in the nano-pores of
631 calcium silicate phase: The influence of calcium to silicate ratios, Microporous
632 Mesoporous Mater. 255 (2018) 23-35.
633 [34] Y. Zhou, D. Hou, J. Jiang, P. Wang, Chloride ions transport and adsorption in the
634 nano-pores of silicate calcium hydrate: Experimental and molecular dynamics studies,
635 Construction and Building Materials 126 (2016) 991-1001.
636 [35] I.G. Richardson, Tobermorite/jennite- and tobermorite/calcium hydroxide-based
637 models for the structure of C-S-H: applicability to hardened pastes of tricalcium silicate,
638 β-dicalcium silicate, Portland cement, and blends of Portland cement with blast-furnace
639 slag, metakaolin, or silica fume, Cement and Concrete Research 34(9) (2004) 1733-
640 1777.
641 [36] M.A.B. Promentilla, T. Sugiyama, T. Hitomi, N. Takeda, Quantification of
642 tortuosity in hardened cement pastes using synchrotron-based X-ray computed
643 microtomography, Cem. Concr. Res. 39(6) (2009) 548-557.
644 [37] E. Gallucci, K. Scrivener, A. Groso, M. Stampanoni, G. Margaritondo, 3D
645 experimental investigation of the microstructure of cement pastes using synchrotron X-
646 ray microtomography (μCT), Cem. Concr. Res. 37(3) (2007) 360-368.
647 [38] R.J.M. Pellenq, N. Lequeux, H. van Damme, Engineering the bonding scheme in
648 C–S–H: The iono-covalent framework, Cem. Concr. Res. 38(2) (2008) 159-174.
649 [39] F. Sanchez, K. Sobolev, Nanotechnology in concrete – A review, Construction and
650 Building Materials 24(11) (2010) 2060-2071.
651 [40] K. Ioannidou, K.J. Krakowiak, M. Bauchy, C.G. Hoover, E. Masoero, S. Yip, F.J.
652 Ulm, P. Levitz, R.J. Pellenq, E. Del Gado, Mesoscale texture of cement hydrates, Proc.
653 Natl. Acad. Sci. U. S. A. 113(8) (2016) 2029-34.
654 [41] B. Šavija, J. Pacheco, E. Schlangen, Lattice modeling of chloride diffusion in
655 sound and cracked concrete, Cem. Concr. Compos. 42 (2013) 30-40.
656 [42] D.P. Bentz, D.A. Quenard, V. Baroghel-Bouny, E.J. Garboczi, H.M. Jennings,
657 Modelling drying shrinkage of cement paste and mortar Part 1. Structural models from
658 nanometres to millimetres, Materials and Structures 28(8) (1995) 450-458.
659 [43] H.M. Jennings, A model for the microstructure of calcium silicate hydrate in
660 cement paste, Cem. Concr. Res. 30(1) (2000) 101-116.
661 [44] V. Morales-Flórez, N.D. Rosa-Fox, M. Piñero, L. Esquivias, The Cluster Model:
662 A Simulation of the Aerogel Structure as a Hierarchically-Ordered Arrangement of
663 Randomly Packed Spheres, J. Sol-Gel Sci. Technol. 35(3) (2005) 203-210.
664 [45] M.A. Etzold, P.J. McDonald, A.F. Routh, Growth of sheets in 3D confinements —
665 a model for the C–S–H meso structure, Cem. Concr. Res. 63 (2014) 137-142.
666 [46] J.W. Bullard, VCCTL Software, https://www.nist.gov/services-
667 resources/software/vcctl-software.
668 [47] Z. Yu, A. Zhou, D. Lau, Mesoscopic packing of disk-like building blocks in
669 calcium silicate hydrate, Sci. Rep. 6 (2016) 36967.

[48] G. Ye, K. van Breugel, A.L.A. Fraaij, Three-dimensional microstructure analysis of numerically simulated cementitious materials, Cem. Concr. Res. 33(2) (2003) 215-222.
[49] S. Bishnoi, K.L. Scrivener, μic: A new platform for modelling the hydration of cements, Cem. Concr. Res. 39(4) (2009) 266-274.
[50] W.B. Jeffrey, E. Edith, L.G. William, G.S. Steven, E.T. Judith, A parallel reaction-transport model applied to cement hydration and microstructure development, Modell. Simul. Mater. Sci. Eng. 18(2) (2010) 025007.
[51] J.G. Ibarra-Armenta, A. Martín-Molina, M. Quesada-Pérez, Testing a modified model of the Poisson–Boltzmann theory that includes ion size effects through Monte Carlo simulations, Phys. Chem. Chem. Phys. 11(2) (2009) 309-316.
[52] Y. Qiao, X. Liu, M. Chen, B. Lu, A Local Approximation of Fundamental Measure Theory Incorporated into Three Dimensional Poisson–Nernst–Planck Equations to Account for Hard Sphere Repulsion Among Ions, J Stat Phys 163(1) (2016) 156-174.
[53] P.M. Biesheuvel, M. van Soestbergen, Counterion volume effects in mixed electrical double layers, J. Colloid Interface Sci. 316(2) (2007) 490-9.
[54] B. Lu, Y.C. Zhou, Poisson-Nernst-Planck equations for simulating biomolecular diffusion-reaction processes II: size effects on ionic distributions and diffusion-reaction rates, Biophys. J. 100(10) (2011) 2475-85.
[55] D. Gillespie, A review of steric interactions of ions: Why some theories succeed and others fail to account for ion size, Microfluid. Nanofluid. 18(5-6) (2014) 717-738.
[56] S.V. Churakov, C. Labbez, L. Pegado, M. Sulpizi, Intrinsic Acidity of Surface Sites in Calcium Silicate Hydrates and Its Implication to Their Electrokinetic Properties, The Journal of Physical Chemistry C 118(22) (2014) 11752-11762.
[57] J. Arnold, D.S. Kosson, A. Garrabrants, J.C.L. Meeussen, H.A. van der Sloot, Solution of the nonlinear Poisson–Boltzmann equation: Application to ionic diffusion in cementitious materials, Cem. Concr. Res. 44 (2013) 8-17.
[58] M. Wang, S. Chen, On applicability of Poisson–Boltzmann equation for micro-and nanoscale electroosmotic flows, Commun Comput Phys 3(5) (2008) 1087-1099.
[59] Y. Yang, M. Wang, Upscaling scheme for long-term ion diffusion in charged porous media, Phys Rev E 96(2-1) (2017) 023308.
[60] S. Succi, Lattice Boltzmann 2038, EPL (Europhysics Letters) 109(5) (2015) 50001.
[61] S. Chen, Z. Wang, X. Shan, G.D. Doolen, Lattice Boltzmann computational fluid dynamics in three dimensions, J Stat Phys 68(3-4) (1992) 379-400.
[62] M. Wang, Structure Effects on Electro-Osmosis in Microporous Media, J. Heat Transfer 134(5) (2012) 051020.
[63] H. Yoshida, T. Kinjo, H. Washizu, Coupled lattice Boltzmann method for simulating electrokinetic flows: A localized scheme for the Nernst–Plank model, Communications in Nonlinear Science and Numerical Simulation 19(10) (2014) 3570-3590.
[64] R.A. Patel, J. Perko, D. Jacques, G. De Schutter, K. Van Breugel, G. Ye, A versatile pore-scale multicomponent reactive transport approach based on lattice Boltzmann

712 method: Application to portlandite dissolution, Physics and Chemistry of the Earth,
713 Parts A/B/C 70–71(0) (2014) 127-137.
714 [65] Z. Chai, C. Huang, B. Shi, Z. Guo, A comparative study on the lattice Boltzmann
715 models for predicting effective diffusivity of porous media, Int. J. Heat Mass Transfer
716 98 (2016) 687-696.
717 [66] H. Yoshida, M. Nagaoka, Multiple-relaxation-time lattice Boltzmann model for the
718 convection and anisotropic diffusion equation, Journal of Computational Physics
719 229(20) (2010) 7774-7795.
720 [67] J.A. Greathouse, R.T. Cygan, J.T. Fredrich, G.R. Jerauld, Adsorption of Aqueous
721 Crude Oil Components on the Basal Surfaces of Clay Minerals: Molecular Simulations
722 Including Salinity and Temperature Effects, The Journal of Physical Chemistry C
723 121(41) (2017) 22773-22786.
724 [68] J. Jiang, P. Wang, D. Hou, The mechanism of cesium ions immobilization in the
725 nanometer channel of calcium silicate hydrate: a molecular dynamics study, Phys.
726 Chem. Chem. Phys. 19(41) (2017) 27974-27986.
727 [69] A.G. Kalinichev, R.J. Kirkpatrick, Molecular Dynamics Modeling of Chloride
728 Binding to the Surfaces of Calcium Hydroxide, Hydrated Calcium Aluminate, and
729 Calcium Silicate Phases, Chem. Mater. 14(8) (2002) 3539-3549.
730 [70] S. Bhattacharya, K.E. Gubbins, Fast Method for Computing Pore Size
731 Distributions of Model Materials, Langmuir 22(18) (2006) 7726-7731.
732 [71] M.Z. Zhang, G. Ye, K. van Breugel, A numerical-statistical approach to
733 determining the representative elementary volume (REV) of cement paste for
734 measuring diffusivity, 2010 60(300) (2010) 14.
735 [72] N. Ukrainczyk, E.A.B. Koenders, Representative elementary volumes for 3D
736 modeling of mass transport in cementitious materials, Modell. Simul. Mater. Sci. Eng.
737 22(3) (2014) 035001.
738 [73] M.H.N. Yio, H.S. Wong, N.R. Buenfeld, Representative elementary volume (REV)
739 of cementitious materials from three-dimensional pore structure analysis, Cem. Concr.
740 Res. 102 (2017) 187-202.
741 [74] T. Pan, Y. Liu, Computational Molecular Analysis of Chloride Transport in
742 Hydrated Cement Paste, Transportation Research Record: Journal of the Transportation
743 Research Board 2113 (2009) 31-40.
744 [75] T. Pan, K. Xia, L. Wang, Chloride binding to calcium silicate hydrates (C-S-H) in
745 cement paste: a molecular dynamics analysis, International Journal of Pavement
746 Engineering 11(5) (2010) 367-379.
747 [76] C. Bucur, M. Olteanu, C. Cristache, M. Pavelescu, Radionuclide transport through
748 cement matrices, Rev. Chim. 61(5) (2010) 458-461.
749 [77] T.C. Hansen, Physical structure of hardened cement paste. A classical approach,
750 Mater. Struct. 19(6) (1986) 423-436.

751